Static and dynamic spin properties in the quantum triangular lattice antiferromagnet Ag$_2$CoO$_2$

H. K. Yoshida,[1] S. E. Dissanayake,[2,*] A. D. Christianson,[2,3] C. R. dela Cruz,[2] Y.-Q. Cheng,[2] S. Okamoto,[3]
K. Yamaura,[4] M. Isobe,[5] and M. Matsuda[2]

[1]*Department of Physics, Hokkaido University, Sapporo 060-0810, Japan*
[2]*Neutron Scattering Division, Oak Ridge National Laboratory, Oak Ridge, Tennessee 37831, USA*
[3]*Materials Science and Technology Division, Oak Ridge National Laboratory, Oak Ridge, Tennessee 37831, USA*
[4]*International Center for Materials Nanoarchitectonics (WPI-MANA), National Institute for Materials Science,*
Tsukuba, Ibaraki 305-0044, Japan
[5]*Research Center for Functional Materials, National Institute for Materials Science, Tsukuba, Ibaraki 305-0044, Japan*

In Ag$_2$CoO$_2$, Co forms triangular lattice layers, which are separated by the metallic (Ag$_2$) block. The magnetic susceptibility and heat capacity measurements show that this material exhibits an antiferromagnetic transition at $T_N = 17.5$ K and the Weiss temperature (T_Θ) and the effective moment are -274 K and 1.62 μ_B, respectively, indicating that the Co ion carries spin (S) 1/2 and has a strongly frustrated state with $T_\Theta/T_N = 15.7$. A density functional theory calculation confirmed that the valence state of the Co ions is 2+ and the low-spin state with $S = 1/2$ is realized at reduced on-site Coulomb interaction on Co. We performed elastic and inelastic neutron scattering experiments in a powder sample of Ag$_2$CoO$_2$. Although no noticeable magnetic Bragg peaks were observed below T_N, distinct magnetic excitations were observed in the inelastic neutron scattering experiments. The excitations are consistent with those expected for the $S = 1/2$ Heisenberg triangular lattice antiferromagnet. These results suggest that the ordered moment is reduced due to the quantum effect, which explains the absence of the magnetic Bragg peaks. Our results thus suggest that Ag$_2$CoO$_2$ is a good candidate to realize a quantum Heisenberg triangular lattice antiferromagnet.

I. INTRODUCTION

Triangular lattice antiferromagnets have been one of the central issues in frustrated magnetism. Prediction of the resonating valence bond (RVB) state [1], a quantum spin liquid state, has triggered vigorous studies to seek unusual magnetic states on the triangular lattice. Although recent theoretical calculations revealed that the ground state of quantum triangular lattice antiferromagnet was an antiferromagnetic long-range ordered state with 120° spin structure [2–4], the ring-exchange interaction or additional interactions sometimes give rise to the quantum spin liquid state [5]. On the other hand, classical triangular antiferromagnets also exhibit exotic magnetic properties depending on the spin anisotropy, such as Kosterlitz-Thouless (KT) transition and chirality ordering for XY spin system [6], and paired to unpaired transition of Z_2 vortices for Heisenberg spin systems [7,8].

In particular, observation of an exotic quantum many-body state such as a quantum spin liquid state, owing to the magnetic frustration and the quantum fluctuation is one of the most intriguing themes in the frustrated magnetism. Thus far, various candidate compounds for a quantum triangular antiferromagnet have been developed including inorganic and organic compounds in which a variety of exotic magnetic phenomena are discussed such as the magnetization plateau,

the spin liquid state [9,10], the quantum disorder state, and the Bose-Einstein condensation of magnon, etc. [11,12]. A recently discovered example is YbMgGaO$_4$ [13,14] in which Yb ions carry spin-1/2 on the triangular lattice. A continuum structure in a magnetic excitation spectrum is observed, which may be evidence of the realization for the quantum spin liquid state. However, potential orientational spin disorder of the Yb ions by site mixing of Mg^{2+} and Ga^{3+} complicates a straightforward interpretation of the data [15]. It is highly desirable to find a new material for the quantum frustrated system.

The Ag$_2$$MO_2$ (M =Cr, Mn, Fe, Ni, Rh) compounds are one of the suitable systems to study the frustrated magnetism on the triangular lattice [16–20]. Figure 1 shows the crystal structure of Ag$_2$$MO_2$ which crystalizes in trigonal symmetry. Each member of the compounds possesses an unusual valence state of (Ag$_2$)$^+$ and M^{3+}. Spins of transition metals localize on the triangular lattice, and a 1/4-filled silver 5s band provides itinerant electrons. Therefore, this system presents a unique playground in which a significant correlation between frustrated spins and itinerant electrons is expected. Previous reports revealed various interesting magnetic properties of series compounds. For instance, the quantum triangular antiferromagnet with $S = 1/2$ Ag$_2$NiO$_2$ shows an orbital ordering of e_g orbital at $T_s = 260$ K which assists a release of magnetic frustration and lead the antiferromagnetic order at $T_N = 54$ K [16], while the more classical system with $S = 3/2$ Ag$_2$CrO$_2$ exhibits the five-sublattice partial disordered state with spontaneous structural distortion at $T_N = 24$ K [19,20].

*Present address: Department of Physics, Duke University, Durham, North Carolina 27708, USA.
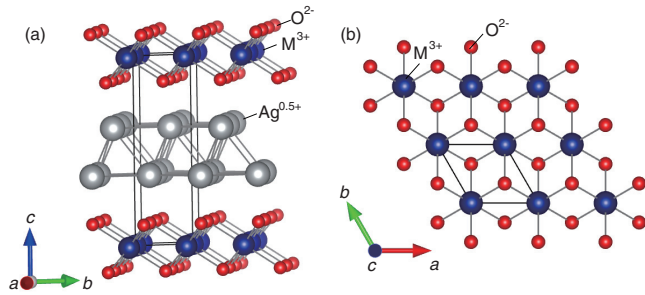
FIG. 1. (a) Schematic illustration of the crystal structure of Ag_2MO_2. (b) Perspective view of the MO_2 plane in which M ions form the equilateral triangular lattice. Co ions occupy the M ion site in this structure.

Recently, we successfully synthesized Ag_2CoO_2 as the new member of Ag_2MO_2. Ag_2CoO_2 has a trigonal structure ($P\bar{3}m1$) with $a = 2.85301$ Å and $c = 8.599731$ Å at $T = 4$ K and the magnetic Co ions consist of regular triangular lattices. In Ag_2MO_2 (M = Cr, Mn, and Ni), the valence state of the transition metal ions is predominantly 3+. If this is also the case in Ag_2CoO_2, the magnetic Co^{3+} ions should carry $S = 0$ [t_{2g}^6, low spin (LS) state], $S = 1$ ($e_g^1 t_{2g}^5$, intermediate spin state), or $S = 2$ [$e_g^2 t_{2g}^4$, high spin (HS) state] according to the balance between the degree of the Hunt coupling and crystal field splitting. The effective paramagnetic moment of Co spins was found to be $p_{eff} = 1.62$ μ_B which was close to the theoretical value for $S = 1/2$ from the magnetic experiments. This spin state is not expected for the usual electron state of Co^{3+} ion. To gain further insights, we performed density functional theory (DFT) calculations and found that Co^{2+} is stabilized in Ag_2CoO_2 by considering the crystal field splitting, Hund coupling, and Coulomb interaction (U). Further, the LS state ($t_{2g}^6 e_g^1$) is realized on Co^{2+} with relatively small onsite U as detailed in Sec. III B. This explains the emergence of $S = 1/2$ in Ag_2CoO_2.

We also performed elastic and inelastic neutron scattering experiments in a powder sample of Ag_2CoO_2. Although a magnetic transition is observed at $T_N = 17.5$ K from the magnetic susceptibility and heat capacity measurements, no noticeable magnetic Bragg peaks were observed below T_N. On the other hand, distinct magnetic excitations were observed at low temperatures in the inelastic neutron scattering experiments. The excitations are very similar to those expected for the $S = 1/2$ Heisenberg triangular lattice antiferromagnet. These results suggest that the magnetic Bragg peaks are not observed in the neutron diffraction data because the ordered moment is suppressed due to quantum effects. Thus, Ag_2CoO_2 is a good candidate for a model compound of a quantum triangular lattice Heisenberg antiferromagnet.

II. EXPERIMENTAL DETAILS

A powder sample of Ag_2CoO_2 was prepared by the high-temperature and high-pressure technique. The stoichiometric mixture of Ag, Ag_2O, and Co_3O_4 reagents were encapsulated in the Pt cell, and it was heated at 900 °C in 6 GPa for 1 h. The temperature dependence of resistivity and heat capacity measurements were performed on the firmly sintered pellet by

the conventional four-probe method and relaxation method, respectively, in a Quantum Design (QD) PPMS. The magnetic properties were measured by using the SQUID magnetometer of a QD MPMS.

The powder sample that weighs ∼4.6 g was used for the elastic and inelastic neutron scattering measurements. The neutron powder diffraction experiments were carried out on the neutron powder diffractometer HB-2A, installed at High Flux Isotope Reactor (HFIR) at Oak Ridge National Laboratory (ORNL). We utilized two wavelengths (λ) 1.5374 and 2.410 Å. An additional diffraction measurement was performed on a triple-axis spectrometer HB-1 at HFIR with a neutron energy of 13.5 meV and a horizontal collimator sequence of 48′-80′-S-80′-240′. Contamination from higher-order beams was effectively eliminated using PG filters. The inelastic neutron scattering experiments were carried out on the chopper neutron spectrometer ARCS [21], installed at the Spallation Neutron Source (SNS) at ORNL. We utilized two incident energies (E_is) of 15 and 40 meV. The energy resolutions at the elastic position for $E_i = 15$ and 40 meV are 0.54 and 1.5 meV, respectively. The measurements were performed in a temperature range of $5 \leqslant T \leqslant 30$ K using a closed-cycle refrigerator. The visualization of the ARCS data were performed using DAVE software [22].

Although the powder samples used for the bulk measurements are free from impurities, the ones for the neutron scattering measurements contain small impurities less than 10%, which originate partly from Ag and Co_3O_4. Ag is nonmagnetic, whereas Co_3O_4 is an antiferromagnet, in which Co^{2+} ($S = 3/2$) and Co^{3+} ($S = 0$) coexist [23]. The Co^{2+} spins, which correspond to 33% of the total Co ions, order antiferromagnetically below 40 K. No magnetic Bragg peaks from Co_3O_4 were observed in the neutron diffraction measurement. These results are consistent with the fact that the averaged Co moment in Co_3O_4 is 1 μ_B, which results in effective impurity moments of ∼0.1 μ_B at most. Moreover, the magnetic susceptibility of the sample used in the neutron scattering experiments shows that the dominant magnetic component is the Ag_2CoO_2. Therefore, we expect that the impurity phases do not yield noticeable effect on the neutron scattering results presented here.

III. RESULTS AND DISCUSSION

A. Magnetic susceptibility, heat capacity, and resistivity

Figure 2(a) shows the temperature dependence of magnetic susceptibility measured in magnetic fields of 0.1, 1, and 5 T. It obeys the Curie-Weiss law in the high temperature region. From the linear extrapolation to the inverse susceptibility above 250 K, the Curie constant and the Weiss temperature were estimated as $C = 0.33$ and $\Theta = -274$ K, respectively. The C value is very close to that for the $S = 1/2$ system. The g factor $g = 1.87$ was estimated from the Curie constant assuming the $S = 1/2$ in the low spin state. The susceptibility suddenly increases below about 20 K, and it tends to saturate with decreasing temperature. This suggests that the compound undergoes magnetic ordering below that temperature. The saturation value of the susceptibility in the magnetic field of 0.1 T at 2 K is 0.031 emu/Co mol. This magnetization
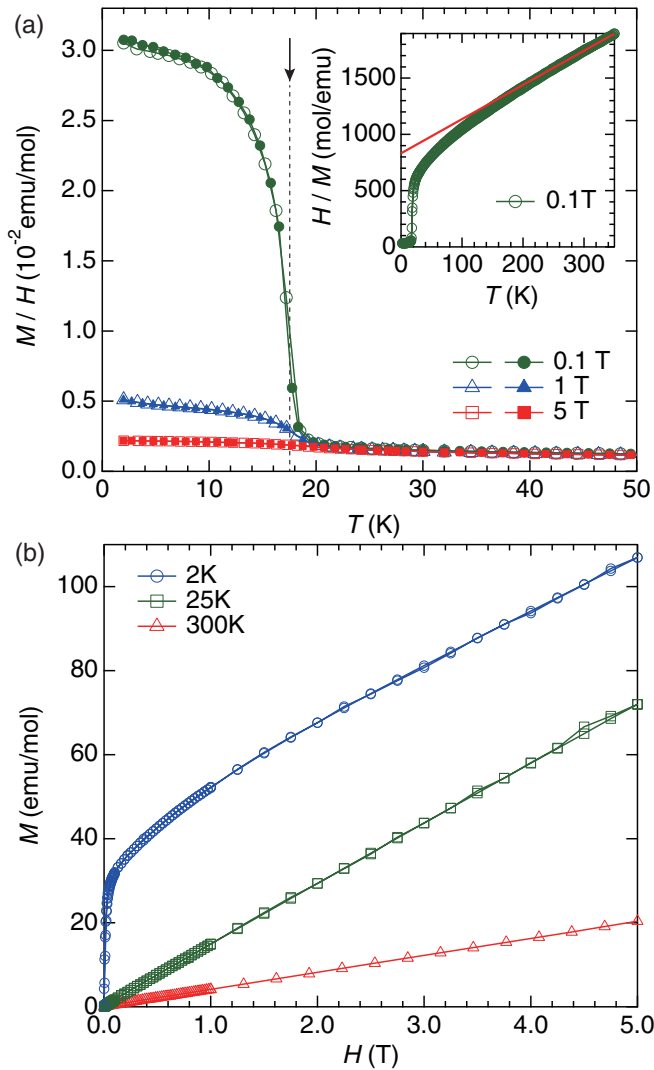
FIG. 2. (a) Temperature dependence of magnetic susceptibility of Ag_2CoO_2 measured in magnetic fields of 0.1 T, 1 T, and 5 T. Zero-field-cooled(ZFC) and field-cooled (FC) process are shown as an open and a solid symbol, respectively. The ZFC process is the heating process after applying each magnetic field at the base temperature, whereas the FC process is the cooling process under the magnetic field. There was no considerable difference between the ZFC and the FC processes. The inset shows the inverse susceptibility. The solid line indicates the result of the linear fitting based on the Curie-Weiss law. The vertical arrow indicates T_N determined from the peak top of the heat capacity. (b) Magnetization curves of Ag_2CoO_2 at temperatures of 2, 25, and 300 K.

FIG. 3. (a) Temperature dependence of heat capacity of Ag_2CoO_2 in C/T vs T plot. The lower inset shows the C/T vs T^2 plot below 10 K. The solid line indicates the linear interpolation below 10 K. The upper inset illustrates the temperature dependence of resistivity of Ag_2CoO_2 below 350 K.

Thus, this phase transition is attributed to the weak ferromagnetic transition. Since there is no suitable compound to estimate the lattice contribution, it is difficult to estimate the magnetic entropy of Ag_2CoO_2. However, the tiny peak in C/T plot shows that the entropy release related to this phase transition is quite small and suggests that almost all of the magnetic entropy is released at higher temperature owing to the low dimensionality of Ag_2CoO_2.

The upper inset of Fig. 3 shows the temperature dependence of resistivity of Ag_2CoO_2. This clearly indicates that the compound has a metallic conductivity. Unlike Ag_2CrO_2 and Ag_2NiO_2 with relatively strong coupling between localized spins and itinerant electrons, there is no anomaly at the magnetic transition in Ag_2CoO_2; the resistivity of Ag_2CrO_2 and Ag_2NiO_2 exhibit a significant reduction at the magnetic transition temperatures [16,19]. The lower inset shows the C/T vs T^2 plot below 10 K. The Sommerfeld coefficient γ was estimated to be 8.22 mJ/molK² from the extrapolation to this plot.

The γ value is much larger than that of normal metal compounds. This enhancement was observed in Ag_2MO_2 series compounds [16,17,19], the origin of which was considered to the orbital hybridization between Co^{2+} layer and Ag_2 layer [24]. For instance, the γ value of Ag_2F which has the same Ag_2 layer structure providing the conducting electrons is quite small, 0.66 mJ/molK² [25]. Previous resonant photoemission spectroscopy experiments on Ni and Mn compounds revealed the existence of the narrow DOS of $3d$ orbital at the Fermi level. The γ values of Cr, Mn, and Ni are 9.74, 20.6, and 18.8 mJ/molK², respectively. The electronic state of each compound is the d^3 HS with $S = 3/2$ for Cr^{3+}, d^4 HS with $S = 4$ for Mn^{3+}, and d^7 LS with $S = 1/2$ for Ni^{3+}; in the case of Mn, Mn^{3+} was confirmed by magnetic susceptibility, whereas $Mn^{2.7+}$ was proposed by the resonant PES [26].

value normalized by the saturated magnetization is 5.9×10^{-3} by assuming the $g = 1.87$, which suggests that the magnetic ordering is a canted-antiferromagnetic transition. Figure 2(b) shows magnetization curves measured at several temperatures. Above 25 K, they show a linear field dependence consistent with the paramagnetic state of the compound, while it exhibits a steep enhancement under low magnetic field at 2 K owing to the canted spin arrangement of the compound.

The temperature dependence of heat capacity is depicted in Fig. 3. We observed a tiny peak in C/T plot at $T_N = 17.5$ K, consistent with the anomaly in the magnetic susceptibility.
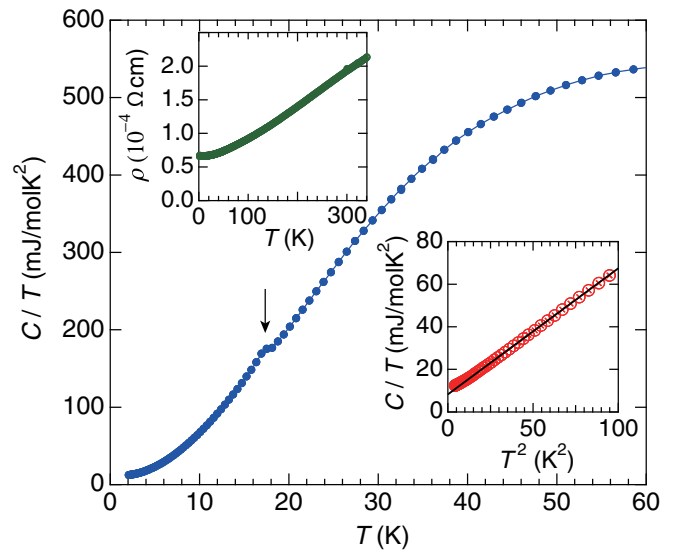
TABLE I. Structural parameters of Ag_2CoO_2 determined by the Rietveld refinements at $T = 4$ K. The trigonal structure with $P\bar{3}m1$ symmetry was used.

Atom	Position	x	y	z	$B_{iso}(\text{Å}^2)$
Ag	$2d$	0.3333	0.6667	0.6315(7)	0.12(6)
Co	$1a$	0.0000	0.0000	0.0000	2.04(33)
O	$2d$	0.6667	0.3333	0.1161(8)	0.81(9)

$a = 2.8537(1)$ Å, $b = 2.8537(1)$ Å, $c = 8.6030(4)$ Å
$R_{Bragg} = 12.7\%$

Extracting some information from these electronic trend should be a key to understand the origin of the enhancement of Ag_2MO_2 system. However, as discussed below, the valence state of Co is suggested to be 2+, and thus the comparison is complicated. The difference in γ value between Co^{2+} and Ni^{3+} in spite of the same electronic state with d^7 LS, showing that the degree of hybridization between triangular layer and Ag_2 layer should be the key ingredient; of course, it may depend on the slight structural discrepancy, and thus it is complicated. The hybridization of localized transition metal and nonmagnetic layer is the inevitable factor for the γ enhancement, and further study of detailed XAS, resonant PES, and theoretical calculation are required to understand the microscopic origin of it.

B. Valence state of the Co ion

To gain insight into the electronic structure of Ag_2CoO_2, we carried out the DFT calculations. We use the generalized gradient approximation and projector augmented wave approach [27] as implemented in the Vienna *ab initio* simulation package (VASP) [28,29]. For each element, we use the standard potential in the VASP distribution. We use the experimental structural parameters as presented in Table I with a $12 \times 12 \times 6$ **k**-point grid and an energy cutoff of 500 eV. To account for correlation effects, the local U is included on the Co d states [30]. Various values are considered, including $U_{Co} = 6.7$ eV and 4.4 eV from Ref. [31] and 3 eV. Since the actual magnetic ground state remains to be fully determined, we consider a ferromagnetic state, which is commensurate with the structural unit cell. Despite this simplicity, we could gain very useful information about electronic and magnetic properties of Ag_2CoO_2.

First, the total charge density on the Co d shell is found to be ≈ 7.1 and rather insensitive to the value of U_{Co}. Thus, the valence state of Co is robustly $+2$. Second, the spin state of Co turns out to be sensitive to U_{Co} and shows a transition at $U_{Co} \sim 4$ eV. Figure 4 shows the DOS computed with $U_{Co} = 4.4$ eV (a) and $U_{Co} = 3$ eV (b). In (a), the Fermi level crosses the minority spin Co d states originating from Co t_{2g}, and the majority spin Co d states are nearly fully filled, realizing the HS state with $t_{2g}^5 e_g^2$. In (b), the Fermi level crosses the majority spin Co d states originating from Co e_g states, and the gap exists between the occupied minority spin Co t_{2g} states and the unoccupied minority spin Co e_g states, realizing the LS state with $t_{2g}^6 e_g^1$. Obtained ordered moment is 3.1 μ_B for (a) and 1.8 μ_B for (b).
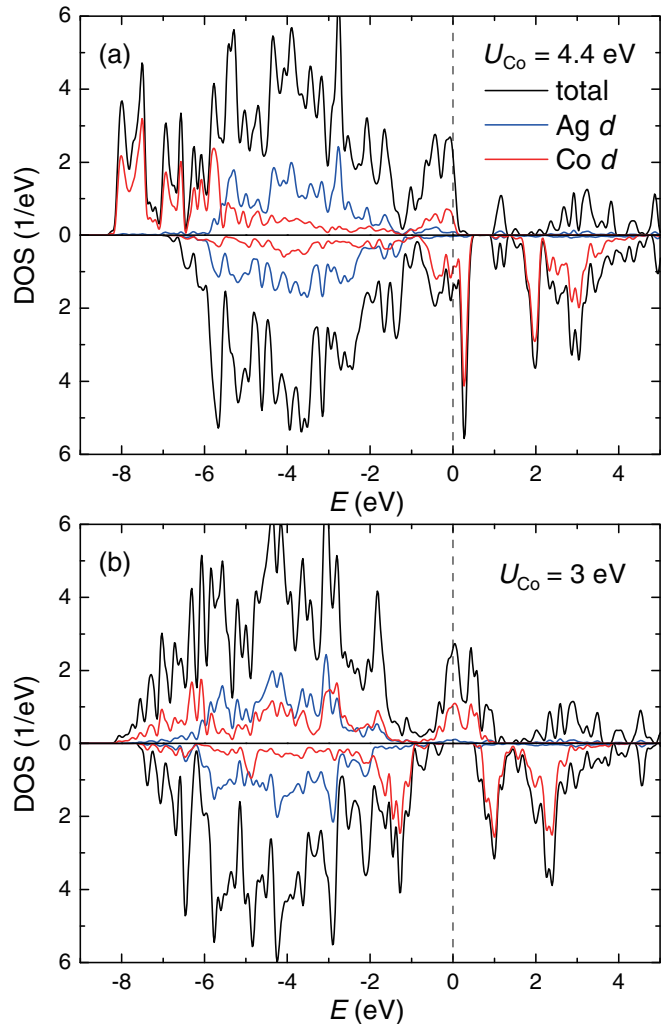

FIG. 4. Density of states of Ag_2CoO_2 computed with $U_{Co} = 4.4$ eV (a) and 3 eV (b). The Fermi level is located at $E = 0$ as indicated by the broken line, and in each graph the upper (lower) panel shows majority (minority) spin states. The HS state with the ordered moment 3.1 μ_B is realized in (a), while the LS state with 1.8 μ_B is realized in (b).

Our DFT result on the LS state appears to be consistent with the experimental findings, but the relatively small $U_{Co} = 3$ eV is required. How could U_{Co} be reduced from a theoretical estimate of 4.4 eV for Co^{2+} [31] by ~ 1 eV? A key ingredient of such a large reduction would be metallic Ag layers adjacent to CoO_2 layers. Because of the metallic layers, the Coulomb repulsive interactions on Co d states could be screened more strongly than in insulating Co oxides as discussed in Ref. [31].

C. Neutron diffraction

Figure 5(a) shows the neutron powder diffraction patterns in Ag_2CoO_2 measured on HB-2A with $\lambda = 2.410$ Å at 4 and 50 K. It is noted that the weak intensity and the high background originate from absorption from Ag and Co atoms and incoherent scattering from Co atoms, respectively. The diffraction patterns are almost identical at the two temperatures, indicating that there are no perceivable magnetic
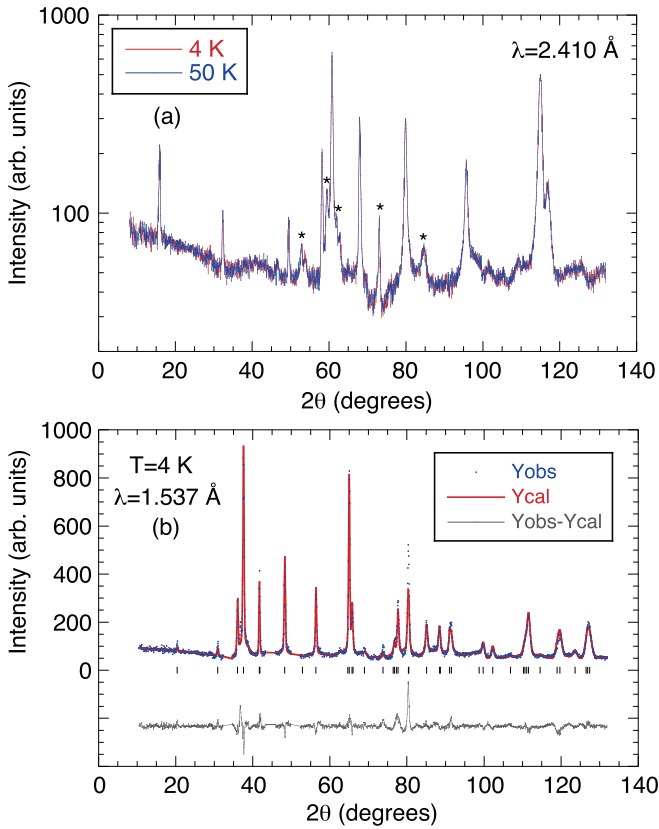
FIG. 6. Color contour maps of the inelastic neutron scattering intensity $S(|Q|, E)$ for Ag_2CoO_2 powder measured with $E_i = 15$ meV at $T = 5$ (a), 15 (b), 18 (c), and 25 K (d).

FIG. 5. (a) Neutron powder diffraction patterns in Ag_2CoO_2 measured with $\lambda = 2.410$ Å at 4 and 50 K. The logarithmic scale is used for the vertical axis. No noticeable difference was observed below and above $T_N(=17.5$ K). "*" denotes that the peaks are from impurity phases. (b) Rietveld refinement of the neutron powder diffraction pattern measured with $\lambda = 1.5374$ Å at $T = 4$ K. Bragg reflections from the impurity phases were excluded in the refinement.

Bragg peaks developing below $T_N = 17.5$ K. As described in Sec. III C, we expect that the negligible magnetic signal is ascribed to the reduced ordered moment due to the quantum effect.

The neutron diffraction data measured on HB-2A with $\lambda = 1.5374$ Å at 4 K, shown in Fig. 5(b), was analyzed to obtain the structural parameters. We performed a Rietveld refinement, using the Fullprof package [32]. In the refinement, trigonal structure with $P\bar{3}m1$ symmetry was assumed. The nuclear Bragg reflections are fitted with the model reasonably well. The Bragg R-factor is 12.7%. The structural parameters determined are shown in Table I. Although the R-factor is somewhat large due to the impurity phase, the DFT calculation using these structural parameters reveals that the structural model is reasonably stabilized (see Appendix), which ensures the results of the powder structural refinement. Of course, we need more precise structural analysis to conclude the detailed crystal structure hopefully using single crystals of Ag_2CoO_2. Although no magnetic Bragg peaks were observed, we estimated the upper limit of the ordered magnetic moment of the Co^{3+} spin from the statistical errors, assuming the 120 degree spin structure with the spins in the ab plane and the spins coupled ferromagnetically along the c axis. This magnetic structure is one of the likely models deduced from
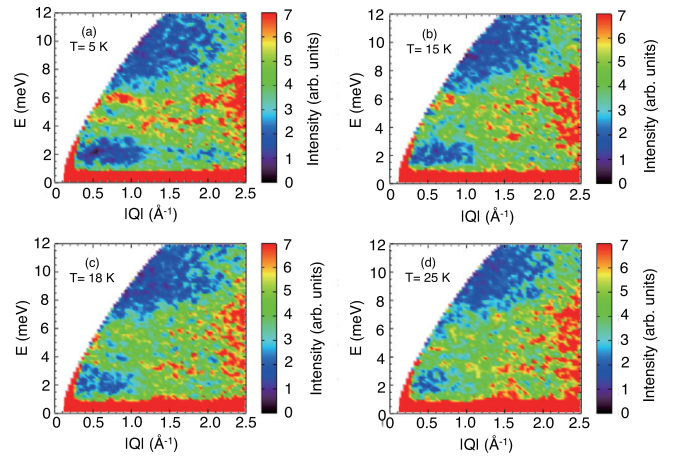
the results of the inelastic neutron measurements described in Sec. III C. An ordered moment of 1 μ_B is calculated to give about 10 counts in Fig. 5(b), which almost corresponds to the error of the background signal. In order to estimate the moment size more accurately, we also performed additional diffraction measurement with high beam flux and low Q resolution on HB-1. Although the nuclear Bragg peak intensities were 30 times more than those observed on HB-2A, distinct magnetic Bragg peaks were not still observed (not shown). From the error of the background signal, the ordered moment is estimated to be 0.6 μ_B at the largest.

D. Inelastic neutron scattering

We performed an inelastic neutron scattering experiment in order to clarify whether the spin wave excitations exist at low temperatures. Figure 6 shows the excitation spectra in Ag_2CoO_2 powder measured on ARCS as a function of temperature. The scattering below ~2 Å^{-1} is distributed up to 8 meV at 25 K ($>T_N$). With decreasing temperature, the spectral weight changes and the intensity below ~3 meV decreases and that above ~4 meV increases.

DFT calculations were performed to estimate the phonon intensities from the sample and also the aluminum sample holder. The details are shown in Appendix. It was confirmed that the region of $Q \leqslant 2$ Å^{-1} and $E \leqslant 10$ meV is free from aluminum phonons. There are optical phonon modes around 5 meV from the sample. However, the intensity of these modes is negligibly weak below 2 Å^{-1}. This is because the phonon intensity scales with Q^2 and the intensity depends on the relative angle between **Q** and the atomic motion directions. From this result, we can safely conclude that the excitation intensities below 1.8 Å^{-1} and 10 meV are of magnetic nature. This is consistent with the estimated background intensities shown in Figs. 7(b) and 7(c). We are also aware that there is a known spurious background around 4 meV and below 0.8 Å^{-1}, originating from the instrument with the same configuration. We avoided using the data in this region for analysis.

In order to distinguish phonon and magnon excitations, we examine Q cuts (Fig. 7) and energy cuts (Fig. 8) of the
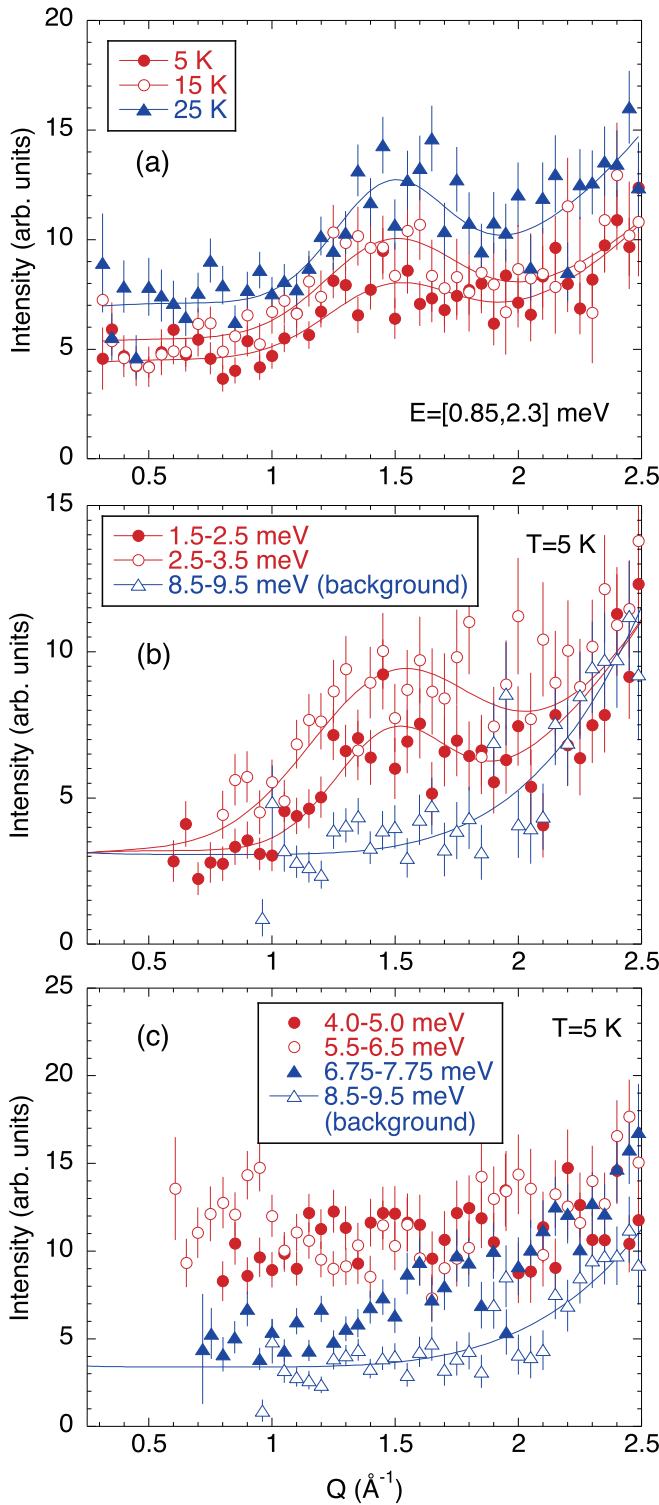
FIG. 7. (a) Q cuts of $S(|Q|, E)$ integrated with respect of energy in the range of $E = 0.85$–2.3 meV measured with $E_i = 15$ meV at $T = 5$, 15, and 25 K. (b) Q cuts of $S(|Q|, E)$ integrated with respect of energy in the range of $E = 1.5$–2.5 meV and 2.5–3.5 meV (b) and 4.0–5.0 meV, 5.5–6.5 meV, and 6.75–7.75 meV (c) measured with $E_i = 15$ meV at $T = 5$ K. The scattering intensity averaged in the energy range between 8.5 and 9.5 meV can be regarded as a background. The solid lines are guides to the eye.
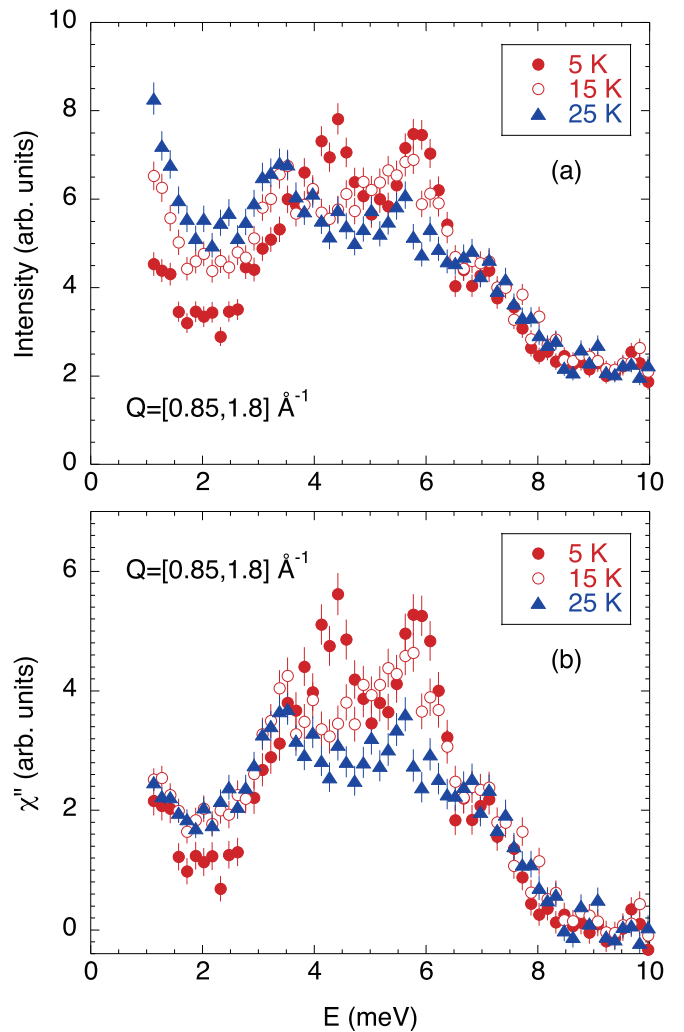

FIG. 8. (a) Energy cuts of $S(|Q|, E)$ integrated with respect of $|Q|$ in the range of $|Q| = 0.85$–1.8 Å^{-1} at $T = 5$, 15, and 25 K. (b) Energy cuts of $\chi''(E)$ converted from the Q integrated $S(|Q|, E)$. The constant background intensity estimated in the energy range between 8.5 and 10 meV was subtracted before the conversion.

observed inelastic neutron intensities. Figure 7(a) shows the Q dependence of the low energy intensities integrated over the energy range between 0.85 and 2.3 meV as a function of temperature. A broad peak near 1.5 Å^{-1} is observed at the same position at temperatures above and below T_N. This peak emanates from the magnetic zone center and hence provides insight into the spin correlations of the magnetic ground state. Since 1.48 Å^{-1} corresponds to the Q value for (1/3, 1/3, 0), the magnetic state is consistent with a 120 degree structure as is typical for triangular lattice materials [33–35].

Figures 7(b) and 7(c) display the Q cuts of the observed intensities as a function of energy at 5 K. As described above, the scattering intensity averaged in the energy range between 8.5 and 9.5 meV can be regarded as a background, which contains phonon scatterings, for a wide energy range below 7.75 meV. Up to 3.5 meV, the broad peak around 1.5 Å^{-1} persists. At energies between 4.0 and 6.5 meV, the intensities

are almost flat as a function of Q. The intensity around 7.25 meV also does not show strong Q dependence.

Figure 8 shows the density of states of the excitations. Since the low-Q region ($0.85 < Q < 1.8$ Å^{-1}), where the phonon contribution is negligible, is integrated, the plots approximately correspond to the magnon density of states. Figures 8(a) and 8(b) represent the scattering intensity and imaginary part of the dynamic susceptibility (χ''), respectively. The characteristic is that both the intensity and the dynamic susceptibility do not show drastic change at T_N but rather a gradual change with temperature. At 5 K, there are two sharp peaks at 4.4 and 5.9 meV and a shoulder around 7 meV. With increasing temperature, both of the sharp peaks shift to lower energies, while the shoulder peak is almost unchanged. The gradual change of the magnetic excitations suggests that the magnetic transition at $T_N = 17.5$ K does not affect the magnetic excitations significantly. This is consistent with the diffraction result where no magnetic Bragg peaks were observed. Since T_Θ is -274 K (23.6 meV), the magnetic correlations are expected to develop two-dimensionally even well above T_N and the spin-wave excitations are already distinct, as is seen in low-dimensional systems [36–38]. The ordered moment can be much reduced so that the modification of the spin-wave excitations due to the three-dimensionally ordered state can be small. The low energy excitation at least down to 0.85 meV is finite at 5 K, indicating that the spin gap is small so that the magnetic anisotropy is small.

Since the excitations become more softened at higher temperatures, effective χ'' around 1 meV should be more enhanced at higher temperatures. This suggests that the excitations between $\sim$3 and $\sim$6.5 meV are transferred to the quasielastic component.

E. Spin-wave calculation

In order to understand the observed magnetic excitations, we performed linear spin-wave calculations for the Hamiltonian of the two-dimensional triangular lattice Heisenberg antiferromagnet with the nearest-neighbor interaction (J). The magnetic ground state of this model is the 120 degree structure. This is consistent with the experimental results that the low-energy excitations are centered at (1/3, 1/3, 0), as described in Sec. III D. SpinW package [39] was used for the calculations. Figure 9(a) shows the spin-wave dispersions along the high-symmetry directions calculated with $J = 4$ meV. The powder averaged magnetic excitation spectra, which were derived from the dispersions, are plotted in Fig. 9(b). Although the flat bandlike feature at 4 and 6 meV is reproduced, the calculated dispersions are sharper than those observed [Fig. 6(a)]. Figure 9(c) represents the integrated intensity in the Q range of $0.85 \leqslant Q \leqslant 1.8$ Å^{-1} as a function of energy, which corresponds to Fig. 8(a). The two-peak structure at $\sim$4 and $\sim$6 meV is consistent with the observed one. The two peaks originate from the band maximum and the local minimum of the spin-wave modes at the M point. The calculation does not reproduce the observed shoulder around 7 meV. These calculations by the linear spin-wave model indicate that the broadening in Q of the dispersions [see Figs. 6(a) and 9(b)] and the additional signal around
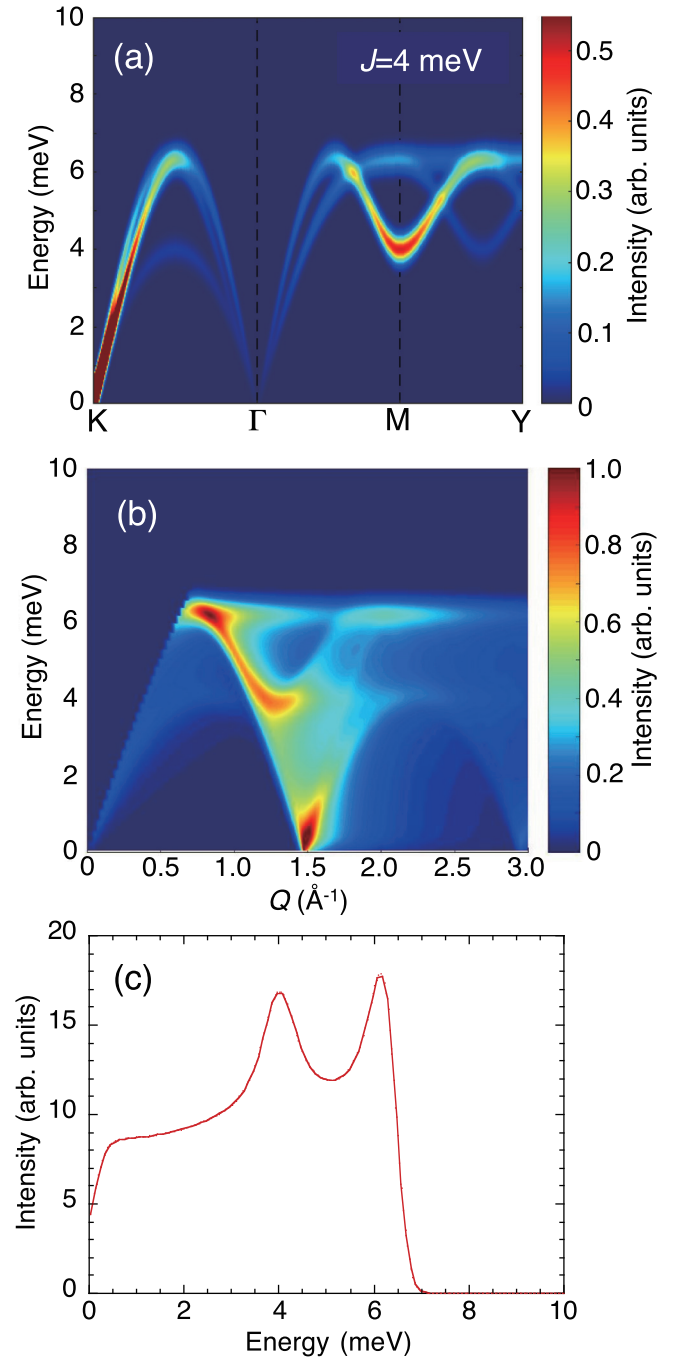

FIG. 9. Results of linear spin-wave calculations for Ag$_2$CoO$_2$ performed using SpinW [39]. (a) Spin-wave dispersions along the high-symmetry directions calculated with $J = 4$ meV. (b) Powder averaged magnetic excitations obtained from (a). Broadening of the excitations (0.54 meV) due to the instrumental resolution is convoluted in (a) and (b). (c) Energy dependence of the intensity integrated over the Q range between 0.85 and 1.8 Å^{-1}.

7 meV are characteristic features in Ag$_2$CoO$_2$ which cannot be explained by the classical model.

We now compare our experimental results with the theoretical ones previously reported, in which interacting spin waves are considered. The spin-wave calculations on the Heisenberg quantum triangular lattice antiferromagnet with $1/S$ correc-

tion shows bound states, which extend to higher energies than those of the single magnon modes [33,34]. The theoretical calculation [34] predicts that the magnon density of states for the $S = 1/2$ system shows relatively sharp peaks around $0.85J$ and $1.25J$ and a broad peak around $1.6J$, which is very similar to the observed one. The first two peaks come from the single magnon modes similar to those in Fig. 9(a) and the third one originates from the two-magnon mode. The enhanced two-magnon mode is a characteristic feature in the quantum triangular lattice antiferromagnets [35,40,41]. Since our data shows peaks at 4.4, 5.9, and 7.0 meV at 5 K, J can be roughly estimated to be ∼4.7 meV, with which the peaks are expected to be observed at 4.0, 5.9, and 7.5 meV. The disagreement of the relative peak positions between the theory and the experiment could originate from further-neighbor interactions, interlayer coupling, and magnetic anisotropy. Our data also shows that the energy positions of the two lower energy peaks are reduced by ∼0.5–0.8 meV at 25 K. This probably corresponds to magnon softening or reduction of the magnetic anisotropy. On the other hand, the intensity and energy of the excitation at 7.0 meV are almost temperature independent. This might suggest that the two-magnon mode with quantum nature is less affected by thermal fluctuations. This could be related to the quantum excitations in other systems. For example, in the $S = 1/2$ Heisenberg antiferromagnetic chain compound $KCuF_3$, it is reported that the high-energy spinon continuum is less temperature dependent, although the low-energy dispersive modes are strongly temperature dependent [36].

As described above, J (=4.7 meV) estimated here is larger than 4.0 meV estimated from the linear-spin-wave theory. This suggests the quantum renormalization of the magnon energies, theoretically predicted [33]. The magnon energies are renormalized by about 15% in this material.

It is noted that J estimated from the magnetic susceptibility result (J_s) is 96 K (=8.3 meV), which is a factor of ∼1.8 larger than that suggested from the neutron scattering results. This disagreement may also be ascribed to the quantum renormalization. If the next-nearest-neighbor (NNN) and interlayer interactions are finite, J_s should change. When these interactions are ferromagnetic, J_s should become larger. However, these interactions are expected to be small because they work to stabilize the long-range magnetic order and the strong frustration with $T_\Theta/T_N = 15.7$ cannot be reached. Therefore, the large difference cannot be explained only from the interactions.

A tiny ferromagnetic component of $5.4 \times 10^{-3} \mu_B$ appears below T_N. Similar weak ferromagnetism was also observed in Ag_2CrO_2 [19,20]. This was ascribed to the partially disordered spins and the magnetization curve exhibits a plateau, where the disordered spins are considered to be aligned to the field direction. On the other hand, no magnetization plateau was observed up to 5 T in Ag_2CoO_2, indicating that the small ferromagnetic component originates from a spin canting. The spin-wave excitation spectrum at 5 K, in which the dispersion stems from (1/3, 1/3, 0), indicates that the overall spin structure is the 120 degree structure in the ab plane and ferromagnetic between the planes. The small spin canting may occur perhaps due to the Dzyaloshinskii-Moriya interactions.

Our results suggest that an antiferromagnetic transition occurs at 17.5 K with a reduced ordered moment due to the quantum fluctuations. The reduction of the ordered moment is expected in the $S = 1/2$ triangular lattice antiferromagnet [4]. In particular, the reduction is large when the interaction is isotropic and a small NNN interaction (⩽0.05J) is present. A possibility of substantial further-neighbor interactions is suggested in Ag_2CrO_2 to explain the partially disordered spin phase [20]. The NNN interaction might also be non-negligible in Ag_2CoO_2.

The discussion above on the inelastic neutron scattering experiments is based on the existence of the long-range magnetic order in Ag_2CoO_2, which is quite reasonable, since the bulk magnetic and heat capacity measurements show clear signatures of a magnetic phase transition. However, we emphasize here that the analysis and discussion made in Secs. III D and III E should be valid even if there is no long-range magnetic order. As described in Sec. III D, the magnetic excitations were measured far below T_Θ [36–38]. Therefore, the observed magnetic excitations should originate from the antiferromagnetic triangular spin layers, in which two-dimensional correlations are well developed.

IV. SUMMARY

We have studied static and dynamic spin properties in a triangular lattice antiferromagnet Ag_2CoO_2. The magnetic excitations are consistent with those expected for the $S = 1/2$ Heisenberg triangular lattice antiferromagnet, which includes bound states as well as single magnon modes. The absence of the magnetic Bragg peaks below T_N probably originates from the reduced ordered moment due to the quantum fluctuations. These results suggest that Ag_2CoO_2 is a good candidate for the quantum Heisenberg triangular lattice antiferromagnet.

APPENDIX: PHONON SCATTERING

Figure 10 shows the inelastic neutron spectra in Ag_2CoO_2 in a wide range of momentum and energy spaces. In order to show the phonon scatterings clearer, the upper end of the intensity scale is set at a large value compared to that in Fig. 6. Figures 10(a) and 10(c) are excitation intensities measured with $E_i = 15$ meV, which show low-energy excitations clearly. On the other hand, Figs. 10(b) and 10(d) measured with $E_i = 40$ meV display an overall feature of the excitations. Phonon scatterings are distinct above 2 Å^{-1}.
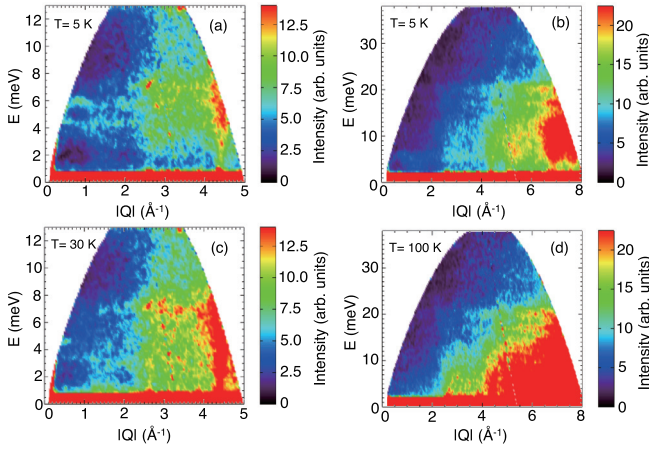
FIG. 10. Color contour maps of the inelastic neutron scattering intensity $S(|Q|, E)$ for Ag_2CoO_2 powder measured at $T = 5$ K with $E_i = 15$ meV (a), at $T = 5$ K with $E_i = 40$ meV (b), at $T = 30$ K with $E_i = 15$ meV(c), and at $T = 100$ K with $E_i = 40$ meV (d).

DFT calculations are performed to simulate the phonon intensities in Ag_2CoO_2. The same parameters as used for the calculations in Sec. III B were used. The calculations were performed with $U = 3$ and 4.4 eV. The results for $U = 3$ eV, which explain the LS state of the Co^{2+} ions, are shown here, although both U values give similar results. The calculation confirms that the crystal structure shown in Fig. 1 and Table I is energetically stable. The phonon dispersions and the density of states are plotted in Figs. 11(a) and 11(b), respectively. Below 10 meV, where we used data for analysis of the magnetic excitations, there are optical phonon modes around 5 meV, which could contribute as a background signal for the magnetic excitations below 1.8 $Å^{-1}$.

The calculated phonon scattering intensity $S(|Q|, E)$ using OCLIMAX [42] for Ag_2CoO_2 powder is shown in Figs. 11(c)–11(f). The plots calculated for $E_i = 40$ meV in Figs. 11(d) and 11(f), which show the overall feature of the phonon scatterings, reproduce the phonon intensities observed experimentally [Figs. 10(b) and 10(d)], although the observed phonons are broader. This is because the actual instrumental resolution is broader. On the other hand, the results calculated for $E_i = 15$ meV are slightly different from those observed experimentally. The phonon energies are shifted to lower energies by about 2 meV. However, even though the calculation do not reproduce the energy scale of some phonon dispersions perfectly, the Q dependence of the phonons should behave similarly. As shown in Figs. 11(c) and 11(e), the phonon contributions are negligible below 1.8 $Å^{-1}$ and 12 meV. This is partly because the phonon intensity scales with Q^2 but also the intensity depends on the relative direction between **Q** and the atomic motion. From this result, we can conclude that the excitation intensities below 1.8 $Å^{-1}$ and 10 meV, which were used to discuss the magnetic excitations, are purely magnetic in origin.

The phonon scatterings from aluminum, which is used as a material for the sample holder, is also calculated using DFT, as shown in Fig. 12. There are no optical phonons below 15 meV and no acoustic phonon modes exist below 2 $Å^{-1}$. Therefore, we conclude that the phonons from the
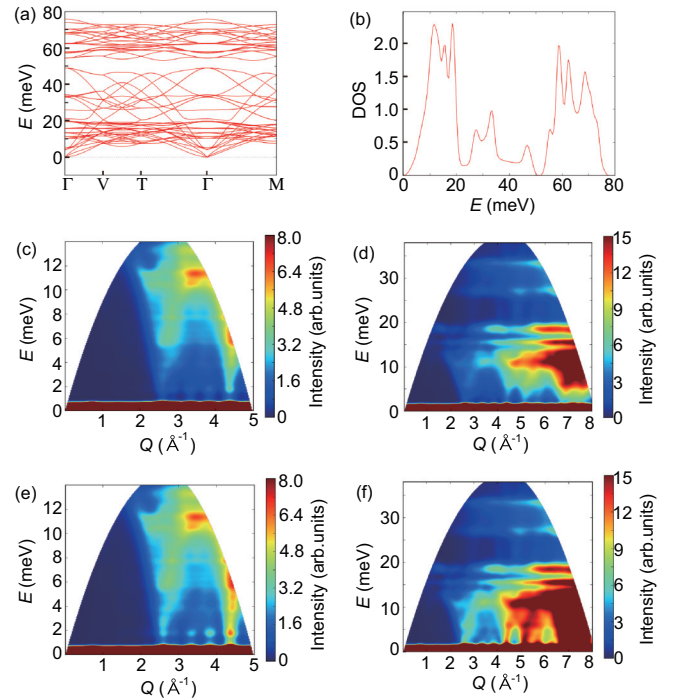

FIG. 11. Phonon calculations performed using DFT with $U = 3$ eV for Ag_2CoO_2. (a) and (b) represent phonon dispersions and phonon density of states, respectively. Color contour maps of the calculated inelastic neutron scattering intensity $S(|Q|, E)$ for Ag_2CoO_2 powder at $T = 5$ K with $E_i = 15$ meV (c), at $T = 5$ K with $E_i = 40$ meV (d), at $T = 30$ K with $E_i = 15$ meV(e), and at $T = 100$ K with $E_i = 40$ meV (f).

aluminum sample holder do not overlap with the magnetic signal from the sample. It is noted that the experimental results does not show strong optical phonon modes around 20 meV, indicating that the background from the sample holder is just minor.
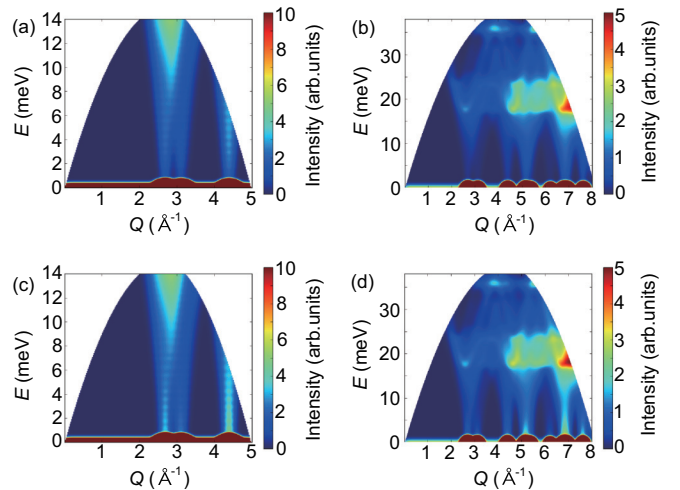

FIG. 12. Color contour maps of the inelastic neutron scattering intensity $S(|Q|, E)$ from phonons in aluminum powder simulated with DFT calculations at $T = 5$ K with $E_i = 15$ meV (a), at $T = 5$ K with $E_i = 40$ meV (b), at $T = 30$ K with $E_i = 15$ meV(c), and at $T = 100$ K with $E_i = 40$ meV (d).

[1] P. W. Anderson, Mat. Res. Bull. **8**, 153 (1973).

[2] B. Bernu, P. Lecheminant, C. Lhuillier, and L. Pierre, Phys. Rev. B. **50**, 10048 (1994).

[3] D. A. Huse and V. Elser, Phys. Rev. Lett. **60**, 2531 (1988).

[4] L. Capriotti, A. E. Trumper, and S. Sorella, Phys. Rev. Lett. **82**, 3899 (1999).

[5] W. LiMing, G. Misguich, P. Sindzingre, and C. Lhuillier, Phys. Rev. B. **62**, 6372 (2000).

[6] S. Miyashita and H. Shiba, J. Phys. Soc. Jpn. **53**, 1145 (1984).

[7] H. Kawamura and S. Miyashita, J. Phys. Soc. Jpn. **53**, 9 (1984).

[8] S. Miyashita and H. Kawamura, J. Phys. Soc. Jpn. **54**, 3385 (1985).

[9] Y. Shimizu, K. Miyagawa, K. Kanoda, M. Maesato, and G. Saito, Phys. Rev. Lett. **91**, 107001 (2003).

[10] S. Yamashita, Y. Nakazawa, M. Oguni, Y. Oshima, H. Nojiri, Y. Shimizu, K. Mitagawa, and K. Kanoda, Nat. Phys. **4**, 459 (2008).

[11] T. Ono, H. Tanaka, H. Aruga Katori, F. Ishikawa, H. Mitamura, and T. Goto, Phys. Rev. B **67**, 104431 (2003).

[12] S. Nakatsuji, Y. Nambu, H. Tonomura, O. Sakai, S. Jonas, C. Broholm, H. Tsunetsugu, Y. Qiu, and Y. Maeno, Science **309**, 1697 (2005).

[13] Y. Shen, Y.-D. Li, H. Wo, Y. Li, S. Shen, B. Pan, Q. Wang, H. C. Walker, P. Steffens, M. Boehm, Y. Hao, D. L. Quintero-Castro, L. W. Harriger, M. D. Frontzek, L. Hao, S. Meng, Q. Zhang, G. Chen, and J. Zhao, Nature (London) **540**, 559 (2016).

[14] J. A. M. Paddison, M. Daum, Z. Dun, G. Ehlers, Y. Liu, M. B. Stone, H. Zhou, and M. Mourigal, Nat. Phys. **13**, 117 (2017).

[15] Z. Zhu, P. A. Maksimov, S. R. White, and A. L. Chernyshev, Phys. Rev. Lett. **119**, 157201 (2017).

[16] H. Yoshida, Y. Muraoka, T. Sorgel, M. Jansen, and Z. Hiroi, Phys. Rev. B **73**, 020408(R) (2006).

[17] H. Yoshida, S. Ahlert, M. Jansen, Y. Okamoto, J. Yamaura, and Z. Hiroi, J. Phys. Soc. Jpn. **77**, 074719 (2008).

[18] S. Ji, E. J. Kan, M.-H. Whangbo, J.-H. Kim, Y. Qiu, M. Matsuda, H. Yoshida, Z. Hiroi, M. A. Green, T. Ziman, and S.-H. Lee, Phys. Rev. B **81**, 094421 (2010).

[19] H. Yoshida, E. Takayama-Muromachi, and M. Isobe, J. Phys. Soc. Jpn. **80**, 123703 (2011).

[20] M. Matsuda, C. de la Cruz, H. Yoshida, M. Isobe, and R. S. Fishman, Phys. Rev. B **85**, 144407 (2012).

[21] D. L. Abernathy, M. B. Stone, M. J. Loguillo, M. S. Lucas, O. Delaire, X. Tang, J. Y. Y. Lin, and B. Fultz, Rev. Sci. Instrum. **83**, 15114 (2012).

[22] R. T. Azuah, L. R. Kneller, Y. Qiu, P. L. W. Tregenna-Piggott, C. M. Brown, J. R. D. Copley, and R. M. Dimeo, J. Res. Natl. Inst. Stan. Technol. **114**, 341 (2009).

[23] W. L. Roth, J. Phys. Chem. Solids **25**, 1 (1964).

[24] M. D. Johannes, S. Streltsov, I. I. Mazin, and D. I. Khomskii, Phys. Rev. B **75**, 180404(R) (2007).

[25] K. Andres, N. A. Kuebler, and M. B. Robin, J. Phys. Chem. Solids. **27**, 1747 (1966).

[26] R. Eguchi, H. Yoshida, Y. Okamoto, A. Chainani, M. Matsunami, Y. Ishida, M. Oura, Y. Senba, H. Ohashi, S. Sshin, and Z. Hiroi, J. Phys. Soc. Jpn. **79**, 023704 (2010).

[27] P. E. Blöchl, Phys. Rev. B **50**, 17953 (1994).

[28] G. Kresse and D. Joubert, Phys. Rev. B **59**, 1758 (1999).

[29] G. Kresse and J. Furthmüller, Phys. Rev. B **54**, 11169 (1996).

[30] S. L. Dudarev, G. A. Botton, S. Y. Savrasov, C. J. Humphreys, and A. P. Sutton, Phys. Rev. B **57**, 1505 (1998).

[31] J. Chen, X. Wu, and A. Selloni, Phys. Rev. B **83**, 245204 (2011).

[32] J. Rodriguez-Carvajal, Physica B **192**, 55 (1993).

[33] A. L. Chernyshev and M. E. Zhitomirsky, Phys. Rev. B **79**, 144416 (2009).

[34] M. Mourigal, W. T. Fuhrman, A. L. Chernyshev, and M. E. Zhitomirsky, Phys. Rev. B **88**, 094407 (2013).

[35] J. Ma, Y. Kamiya, T. Hong, H. B. Cao, G. Ehlers, W. Tian, C. D. Batista, Z. L. Dun, H. D. Zhou, and M. Matsuda, Phys. Rev. Lett. **116**, 087201 (2016).

[36] B. Lake, D. A. Tennant, C. D. Frost, and S. E. Naglar, Nat. Matter. **4**, 329 (2005).

[37] T. Huberman, D. A. Tennant, R. A. Cowley, R. Coldea, and C. D. Frost, J. Stat. Mech.: Theory Exp. (2008) P05017.

[38] A. Mezio, L. O. Manuel, R. R. P. Singh A. E. Trumper, New. J. Phys. **14**, 123033 (2012).

[39] S. Toth and B. Lake, J. Phys.: Condens. Matter **27**, 166002 (2015).

[40] S. Ito, N. Kurita, H. Tanaka, S. Ohira-Kawamura, K. Nakajima, S. Itoh, K. Kuwahara, and K. Kakurai, Nat. Commun. **8**, 235 (2017).

[41] Y. Kamiya, L. Ge, T. Hong, Y. Qiu, D. L. Quintero-Castro, Z. Lu, H. B. Cao, M. Matsuda, E. S. Choi, C. D. Batista, M. Mourigal, H. D. Zhou, and J. Ma, Nat. Commun. **9**, 2666 (2018).

[42] Y. Q. Cheng, L. L. Daemen, A. I. Kolesnikov, and A. J. Ramirez-Cuesta, J. Chem. Theory Comput. **15**, 1974 (2019).